The Astrophysical Journal, 879:5 (12pp), 2019 July 1 https://doi.org/10.3847/1538-4357/ab223b

Particle Acceleration in Kinetic Simulations of Nonrelativistic Magnetic Reconnection with Different Ion–Electron Mass Ratios

Xiaocan Li[1], Fan Guo[1,2], and Hui Li[1]
[1] Los Alamos National Laboratory, Los Alamos, NM 87545, USA; xiaocanli@lanl.gov
[2] New Mexico Consortium, Los Alamos, NM 87544, USA
Received 2019 March 29; revised 2019 May 10; accepted 2019 May 15; published 2019 June 26

Abstract

By means of fully kinetic particle-in-cell simulations, we study whether the proton-to-electron mass ratio m_i/m_e influences the energy spectrum and underlying acceleration mechanism during magnetic reconnection. While kinetic simulations are essential for studying particle acceleration during magnetic reconnection, a reduced m_i/m_e is often used to alleviate the demanding computing resources, which leads to artificial scale separation between electron and proton scales. Recent kinetic simulations with high mass ratios have suggested new regimes of reconnection, as electron pressure anisotropy develops in the exhaust region and supports extended current layers. In this work, we study whether different m_i/m_e changes the particle acceleration processes by performing a series of simulations with different mass ratio ($m_i/m_e = 25$–400) and guide field strength in a low-β plasma. We find that mass ratio does not strongly influence reconnection rate, magnetic energy conversion, ion internal energy gain, plasma energization processes, ion energy spectra, and the acceleration mechanisms for high-energy ions. Simulations with different mass ratios are different in electron acceleration processes, including electron internal energy gain, electron energy spectrum, and the acceleration efficiencies for high-energy electrons. We find that high-energy electron acceleration becomes less efficient when the mass ratio gets larger because the *Fermi*-like mechanism associated with particle curvature drift becomes less efficient. These results indicate that when particle curvature drift dominates high-energy particle acceleration, the further the particle kinetic scales are from the magnetic field curvature scales ($\sim d_i$), the weaker the acceleration will be.

Key words: acceleration of particles – magnetic reconnection – Sun: corona – Sun: flares

1. Introduction

In many solar, space, and astrophysical systems, magnetic reconnection is a major mechanism for energizing plasmas and accelerating nonthermal particles (Zweibel & Yamada 2009). A remarkable example is solar flares, where reconnection is observed to trigger efficient magnetic energy release (Lin & Hudson 1976), heat the coronal plasma (e.g., Caspi & Lin 2010; Longcope et al. 2010), and accelerate both electrons and ions into nonthermal power-law energy distributions (Shih et al. 2009; Krucker et al. 2010; Oka et al. 2013, 2015; Krucker & Battaglia 2014). However, how particles are accelerated over a large-scale reconnection region is still not well understood.

The dynamics of magnetic reconnection is believed to involve both the macroscopic scales ($>10^6$ m in solar flares) and the kinetic scales (<10 m in solar flares; Daughton et al. 2009; Ji & Daughton 2011), and thus a multiscale approach is essential for understanding particle acceleration during reconnection. Starting from the kinetic scales, kinetic simulations (fully kinetic or hybrid) are often used to study how particles are accelerated and coupled with background fluids (e.g., Drake et al. 2006). Various models are then developed to capture these processes for studying the macroscopic particle acceleration (Zank et al. 2014, 2015; le Roux et al. 2015, 2016, 2018; Montag et al. 2017; Drake et al. 2019; Li et al. 2018b) and are applied in explaining local particle acceleration between interacting flux ropes in the solar wind (Zhao et al. 2018, 2019; Adhikari et al. 2019). Previous kinetic simulations have identified that the reconnection X-line region (Hoshino et al. 2001; Drake et al. 2005; Fu et al. 2006; Oka et al. 2010; Egedal et al. 2012, 2015; Wang et al. 2016) and contracting and merging magnetic islands (Drake et al. 2006, 2013; Oka et al. 2010; Liu et al. 2011; Nalewajko et al. 2015) are the major particle acceleration sites during reconnection. Under the guiding-center approximation, recent simulations have also identified particle curvature drift motion along the motional electric field as the major particle acceleration mechanism (Dahlin et al. 2014; Guo et al. 2014, 2015; Li et al. 2015, 2017). Li et al. (2018a) further showed that the flow compression and shear effects capture the primary particle energization well, as in the standard energetic particle transport theory (Parker 1965; Zank 2014; le Roux et al. 2015). Fluid compression and shear effects have also been used to quantify plasma energization during the island coalescence problem (Du et al. 2018). The connection between particle acceleration associated with particle drift motion and that related to fluid motion is summarized in Appendices A and B. Li et al. (2018a) also found that flow compression and shear are suppressed as the guide field increases. To alleviate the computational cost, these previous simulations were mostly carried out using a reduced proton-to-electron mass ratio $m_i/m_e = 25$.

A higher mass ratio ($m_i/m_e \geqslant 400$), however, can potentially change the plasma energization and particle acceleration processes, because different magnetic field, currents, and pressure anisotropy structures emerge as m_i/m_e becomes larger (e.g., Egedal et al. 2013, 2015; Le et al. 2013). By performing kinetic simulations of reconnection with different mass ratio, guide field, and plasma β, Le et al. (2013) demonstrated that the magnetic fields and currents fall into four regimes, and that the transition guide field between different regimes changes with the mass ratio and plasma β. They also identified a new regime with an extended current layer only when $m_i/m_e \geqslant 400$. Those works were mostly focused on the dynamics and structures in the reconnection layer. Therefore, it

is worthwhile to understand how the mass ratio influences the plasma energization and particle acceleration processes.

In this paper, we focus on the consequences of having a disparity between the energy releasing scale (the radius of magnetic curvature $\sim$ the ion inertial length d_i) and the plasma kinetic scales (the electron gyroradius ρ_e to d_i). The scale separation between electrons and protons becomes larger as the mass ratio approaches the realistic value. For example, $\rho_e/d_i = \sqrt{\beta_i}\sqrt{T_e/T_i}\sqrt{m_e/m_i}$ decreases with m_i/m_e, where the ion plasma β_i and the temperature ratio T_e/T_i are usually fixed.

Here we perform fully kinetic particle-in-cell simulations with $m_i/m_e = 25$, 100, and 400 to study whether the mass ratio changes the plasma energization and particle acceleration processes during magnetic reconnection. For each mass ratio, we perform four runs with different guide fields: 0, 0.2, 0.4, and 0.8 times the reconnection magnetic field, so the series of simulations covers all the regimes studied by Le et al. (2013). In Section 2, we describe the simulation parameters. In Section 3, we present the results on how the energy conversion, reconnection rate, particle energy spectra, plasma energization processes, and particle acceleration rates change with the mass ratio and the guide field strength. In Section 4, we discuss the conclusions and the implications based on our simulation results.

2. Numerical Simulations

We carry out 2D kinetic simulations using the VPIC particle-in-cell code (Bowers et al. 2008), which solves Maxwell's equations and the relativistic Vlasov equation. The simulations start from a force-free current sheet with $\boldsymbol{B} = B_0\tanh(z/\lambda)\hat{x} + B_0\sqrt{\mathrm{sech}^2(z/\lambda) + b_g^2}\,\hat{y}$, where B_0 is the strength of the reconnecting magnetic field, b_g is the strength of the guide field B_g normalized by B_0, and λ is the half-thickness of the current sheet. Note that for this paper we will use B_g and b_g interchangeably when it does not cause confusion. We perform simulations with $B_g = 0.0$, 0.2, 0.4, and 0.8 in three mass ratios: 25, 100, and 400. All simulations have the same Alfvén speed v_A ($=B_0/\sqrt{4\pi n_0 m_i}$) and electron beta $\beta_e = 8\pi nkT_e/B_0^2$ defined using reconnecting component of the magnetic field. We choose $\lambda = d_i$ for all simulations, where $d_i = c/\omega_{pi} = c/\sqrt{4\pi n_i e^2/m_i}$ is the ion inertial length. The initial particle distributions are Maxwellian with uniform density n_0 and temperature $T_i = T_e = T_0$. The temperature is taken to be $kT_0 = 6.25\times10^{-4}m_ec^2$, $0.0025m_ec^2$, and $0.01m_ec^2$ for runs with $m_i/m_e = 25$, 100, and 400, respectively, where $m_e\,c^2$ is fixed for runs with different mass ratios. Electrons are set to have a bulk velocity drift U_e so the Ampere's law is satisfied. The ratio of electron plasma frequency and electron gyrofrequency $\omega_{pe}/\Omega_{ce} = 4$, 2, and 1 for runs with $m_i/m_e = 25$, 100, and 400, respectively. The resulting Alfvén speed is $0.05c$ and the electron beta is 0.02 for all simulations. The domain sizes are $L_x\times L_z = 100d_i\times 50d_i$, and the grid sizes are 8192×4096 for all simulations. Figure 1 shows that the electron kinetic scales (ρ_e and d_e) deviate more from the energy releasing scale ($\sim d_i$) as the mass ratio becomes larger. We use 400 particles per cell per species in all simulations. As the mass ratio increases, both the plasma skin depth and gyroradius are at scales shorter than one ion skin depth. For electric and magnetic fields, we employ periodic boundaries along the x-direction and perfectly conducting boundaries along the z-direction. For particles, we employ periodic boundaries along the x-direction and reflecting boundaries along the z-direction. Initially, a long wavelength perturbation with $B_z = 0.02B_0$ is added to induce reconnection (Birn et al. 2001). The simulations are terminated around $t\Omega_{ci} = 100$ (one Alfvén crossing time) to minimize the effect of the periodic boundary conditions along the x-direction.

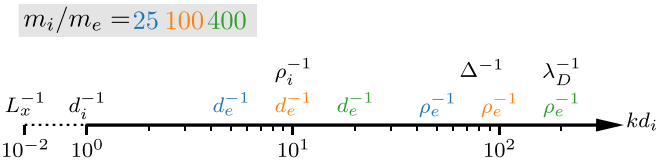

Figure 1. Spatial scales normalized by the ion inertial length d_i in the simulations with different mass ratio m_i/m_e. $d_e = c/\omega_{pe}$ is the electron inertial length. $\rho_e = v_{the}/\Omega_{ce}$ is the electron gyroradius. $\rho_i = v_{thi}/\Omega_{ci}$ is the ion gyroradius, which is the same in terms of d_i for different m_i/m_e. λ_D is the Debye length, which is the same for different m_i/m_e. Δ is the simulation cell size. We also include L_x^{-1}, which is $0.01d_i^{-1}$, in the plot.

3. Results

3.1. Current Layer Structures

As the simulations proceed, current layers are unstable to the tearing instability, leading to fractional sheets filled with magnetic islands. Figure 2 shows the out-of-plane current density j_y for runs with three mass ratios 25–400 with different guide fields from $B_g = 0$ to 0.8. The time steps shown are $t\Omega_{ci} = 80$, 83, and 86 for $m_i/m_e = 25$, 100, and 400, respectively. We choose slightly different time frames because reconnection onsets slightly faster in the runs with a lower mass ratio. Overall, the current layers vary in length and are oriented along different directions depending on the guide field strength. In the low guide field regime, an elongated current layer emerges because of an unmagnetized electron jet formed in the electron diffusion region (panels (b), (e), (f), and (i)). Since there is a finite B_y field in the center of a force-free current sheet even when $B_g = 0$, electrons could be magnetized in the low guide field regime, and localized current layers are formed instead (panels (a) and (j)). A new regime, first studied by Le et al. (2013), emerges with extended current layers embedded in the reconnection exhaust when $m_i/m_e \geqslant 400$ (panel (k)). These current layers can extend over $20d_i$ and therefore might affect particle energization processes. In contrast, the current layers are shorter in runs with a lower mass ratio (panels (c) and (d)). As the guide field gets even stronger (panels (d), (h), and (l)), the electrons become well magnetized, and the current density tends to peak at one of the diagonal branches of the reconnection separatrix. Le et al. (2013) studied the scaling extensively and found that these structures are regulated by the electron pressure anisotropy and the properties of the electron orbits, which depend on the mass ratio and guide field. The scaling in our simulations does not exactly match with the diagram by Le et al. (2013; Figure 3 in their paper). This is because the force-free current sheet (different from the Harris current sheet used in Le et al. 2013) has a finite magnetic field along the guide field direction in the center of the current sheet even when $B_g = 0$, and also because these structures are dynamic and can be destroyed as the simulations evolve. In summary, different mass ratios result in different types of current layers, especially when $B_g \leqslant 0.4$. In the following sections we will study whether the mass ratio dependence

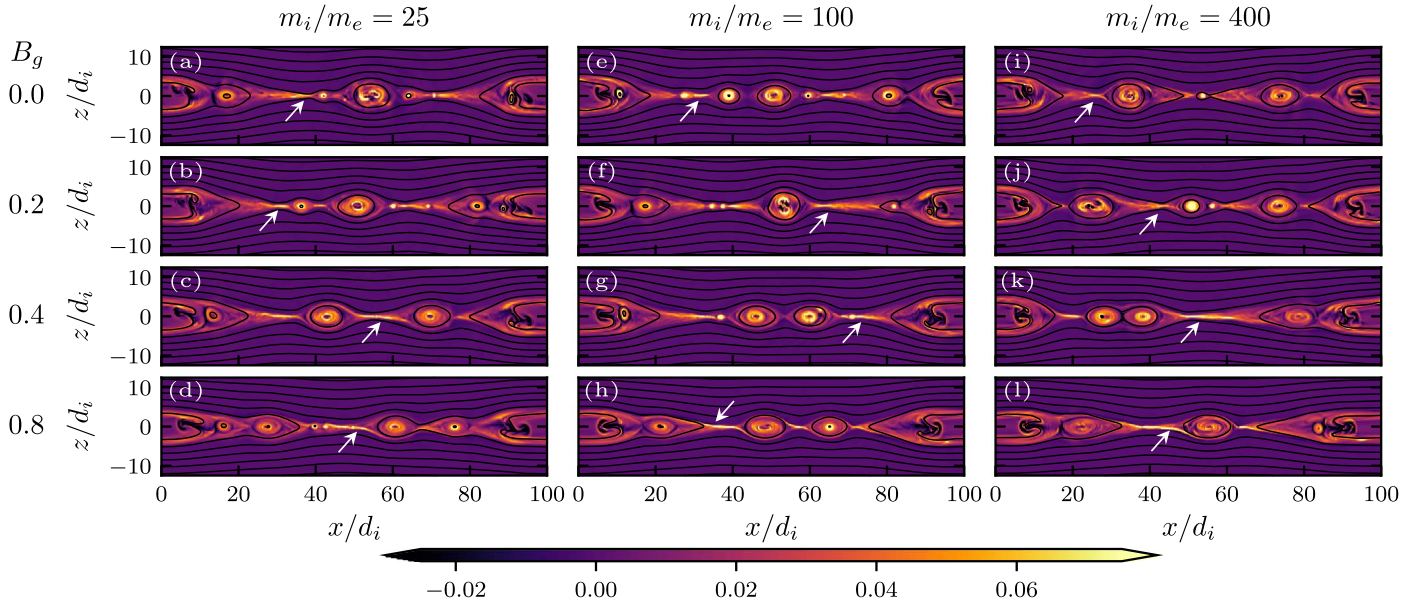

Figure 2. Out-of-plane current density j_y at $t\Omega_{ci} = 80$, 83, and 86 for $m_i/m_e = 25$, 100, and 400, respectively. We choose different time frames because the reconnection onset is faster in the runs with lower mass ratios (see Figure 3). The unit of j_y is en_0c. The white arrows point out regions that are discussed in the main text.

influences the mechanisms for plasma energization and particle acceleration processes.

3.2. Reconnection Rate

Before diving into the energization processes, we check whether the different mass ratio changes the reconnection rate. Following Daughton et al. (2009), we evaluate the normalized reconnection rate $E_R \equiv (\partial\psi/\partial t)/(B_0 v_A)$, where $\psi = \max(A_y) - \min(A_y)$ along $z = 0$, A_y is the y component of the vector potential, and $v_A \equiv B_0/\sqrt{4\pi n_0 m_i}$ is the Alfvén speed defined by B_0 and the initial particle number density n_0. Figure 3 shows that the reconnection rate for various cases. Since we do not average the rate over a long time interval (Daughton et al. 2009), the rate fluctuates rapidly. Figure 3 shows that the reconnection onset is faster in the runs with a lower mass ratio. In the following analysis, unless specified otherwise, we will shift the runs with $m_i/m_e = 100$ by $-3\Omega_{ci}^{-1}$ and the runs with $m_i/m_e = 400$ by $-6\Omega_{ci}^{-1}$ to match the reconnection onset. Figure 3 shows that the reconnection rate is roughly the same for runs with different mass ratios. The peak reconnection rate is about 0.1 for runs with $B_g \leqslant 0.4$, consistent with previous kinetic simulations (e.g., Birn et al. 2001). The peak rate is not sustained, because the periodic boundary conditions limit the simulation durations (Daughton et al. 2006), and because we use the upstream plasma parameters (B_0 and n_0) instead of that near the dominant reconnection x point (Daughton & Karimabadi 2007). At $t\Omega_{ci} = 100$ (one Alfvén crossing time), E_R decreases to about 0.06. We will terminate our analysis at $t\Omega_{ci} = 100$, when only a few large islands and smaller secondary islands are left in the simulations.

The evolution of reconnection rate shows that the runs are similar in the reconnected magnetic fluxes. Previous kinetic simulations have shown that the converted magnetic energy can be channeled into plasma kinetic energy preferentially by the parallel electric field $\boldsymbol{E}_\parallel$ near the reconnection X-line and by the *Fermi*-like mechanism associated with contracting and merging magnetic islands (e.g., Dahlin et al. 2014; Guo et al. 2014; Li et al. 2015, 2017). $\boldsymbol{E}_\parallel$ accelerates particles proportionally to their velocities; the *Fermi*-like mechanisms accelerate particles proportionally to their energies. The dominant mechanism could be different for particles with different energies and for electrons and ions. The mass ratio could change the relative importance of these mechanisms, leading to different particle energy distributions and energy partition between electrons and ions. The following analysis will show how the mass ratio changes the plasma energization and particle acceleration processes.

3.3. Energy Conversion

We start investigating the energization processes by examining the energy evolution in the simulations. Figure 4 shows the energy conversion in these simulations until $t\Omega_{ci} = 100$. Panel (a) shows the time evolution of the change of the magnetic energy $\Delta\varepsilon_B$, the electron energy gain ΔK_e, and the ion energy gain ΔK_i in the runs with $B_g = 0.2$. We normalize them by the initial energy of the x component (reconnecting component) of the magnetic field $\varepsilon_{Bx0} = B_x^2/(8\pi)$. Similar fraction of magnetic energy (11% of ε_{Bx0}) is converted into plasma kinetic energy in all runs. Panel (b) shows that slightly more magnetic energy is converted in runs with $m_i/m_e = 25$ and 400 when $B_g = 0.0$ or 0.8, and similar fractions of magnetic energy are converted for the other cases. Panel (a) shows that as m_i/m_e gets larger, electrons gain less energy, resulting in about 31%, 28%, and 21% of $\Delta\varepsilon_B$ going into electrons in the runs with $m_i/m_e = 25$, 100, and 400, respectively. Panel (b) shows that the difference gets smaller as B_g increases. When $B_g = 0.8$, electrons gain a similar fraction of converted magnetic energy in runs with different mass ratios. Panel (a) also shows that ions gain less energy first and then more energy to the end of the simulation with $m_i/m_e = 400$. Panel (b) shows that ions do gain more energy in runs with $m_i/m_e = 400$ than the other runs, except when $B_g = 0.8$, ions gain most energy in the run with $m_i/m_e = 25$. The guide field dependence of different energies shown in panel (b) is

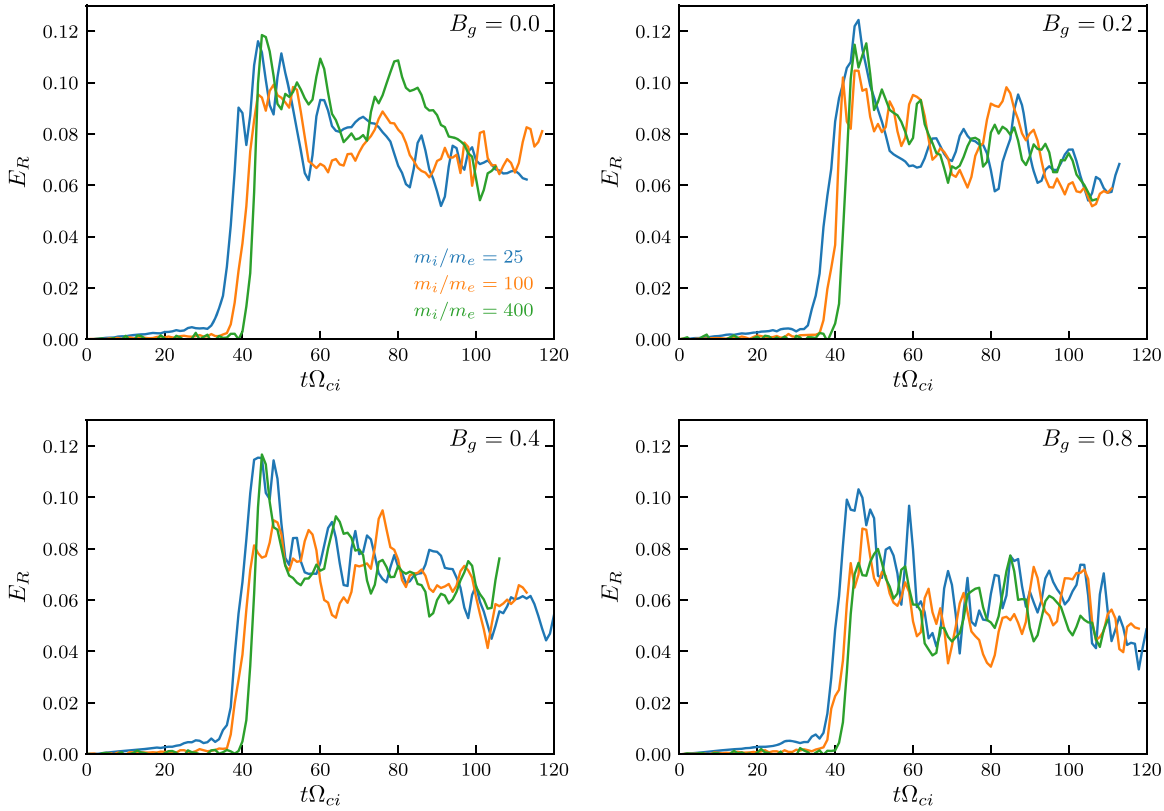

Figure 3. Normalized reconnection rate $E_R = (\partial\psi/\partial t)/(B_0 v_A)$ (Daughton et al. 2009), where $\psi = \max(A_y) - \min(A_y)$ along $z = 0$, A_y is the y component of the vector potential, B_0 is the strength of the initial reconnecting component of the magnetic field, and $v_A \equiv B_0/\sqrt{4\pi n_0 m_i}$ is the Alfvén speed defined by B_0 and the initial particle number density n_0.

consistent for different mass ratios despite the differences in their actual values.

Since the reconnection outflow is about the Alfvén speed $0.05c$, the ion bulk energy is significant in our simulations. Panel (c) shows that, depending on the guide field, the ion bulk energy is comparable with or even larger than the ion internal energy. Panel (c) also shows that the ion bulk energy is larger in the runs with $m_i/m_e = 400$ except when $B_g = 0.8$, and that it does not change much with the guide field when $m_i/m_e = 25$, while it generally gets weaker as m_i/m_e becomes larger. In contrast, the ion internal energy always decreases as B_g gets larger, and the difference between different mass ratio is subtle. As a result, $\Delta K_i/\Delta K_e$ does not show clear dependence on the guide field, while $\Delta U_i/\Delta U_e$ decreases as B_g becomes larger (panel (d)). When $B_g = 0.8$, $\Delta U_i/\Delta U_e$ approaches one for the cases with $m_i/m_e = 100$ or 400 and becomes even smaller in the run with $m_i/m_e = 25$. Panel (d) also shows that $\Delta U_i/\Delta U_e$ is much larger in runs with a higher mass ratio, especially in the low guide field cases. We expect $\Delta U_i/\Delta U_e$ will be even larger in simulations with a real $m_i/m_e = 1836$. In summary, a lower mass ratio helps reconnection to convert more magnetic energy into electron kinetic energy and a similar amount of magnetic energy into ion internal energy, which changes the energy partition between electrons and ions. Then, the next question is whether a different mass ratio results in different electron distributions but similar ion distributions, which we now discuss.

3.4. Particle Energy Distributions

Figure 5 shows the normalized electron energy spectra for all electrons at $t\Omega_{ci} = 40$, 60, and 94. Electrons are accelerated to over 100 times the initial thermal energy $\varepsilon_{\rm th}$ in all runs. The accelerated electrons develop a significant high-energy tail ($>10\varepsilon_{\rm th}$), which contains 0.7%–4% of all electrons and 7%–38% of the total electron kinetic energy to the end of the simulations ($t\Omega_{ci} = 100$). Top panels show that electrons quickly reach $100\varepsilon_{\rm th}$, and that the acceleration is faster in the runs with $m_i/m_e = 100$ or 400. As studied by previous kinetic simulations, parallel electric field $\boldsymbol{E}_\parallel$ plays a key role in the acceleration, for that $E_\parallel$ not only accelerates most electrons near the reconnection X-line (Li et al. 2017; Lu et al. 2018) but also forms pseudo electric potential wells, which trap electrons so that they can be further accelerated by perpendicular electric field $\boldsymbol{E}_\perp$ (Egedal et al. 2015). As a result, most electrons near the X-line are accelerated to develop flat spectra that appear to be hard power-law distributions for $\varepsilon \in [20, 50]\varepsilon_{\rm th}$ (Li et al. 2015). But these spectra are usually transient, because they only contain less than 10% of the high-energy electrons ($>10\varepsilon_{\rm th}$) at $t\Omega_{ci} = 100$, and because these electrons are trapped near the center of the primary magnetic islands (Li et al. 2017). As the simulations evolve to $t\Omega_{ci} = 60$ (panels (e)–(h)), the electron acceleration in the runs with $m_i/m_e = 25$ catches up and becomes the strongest, especially in runs with $B_g = 0.4$ or 0.8 (panels (g) and (h)). The spectra appear to be power-law distributions with a power index -3.5 (dashed lines) for

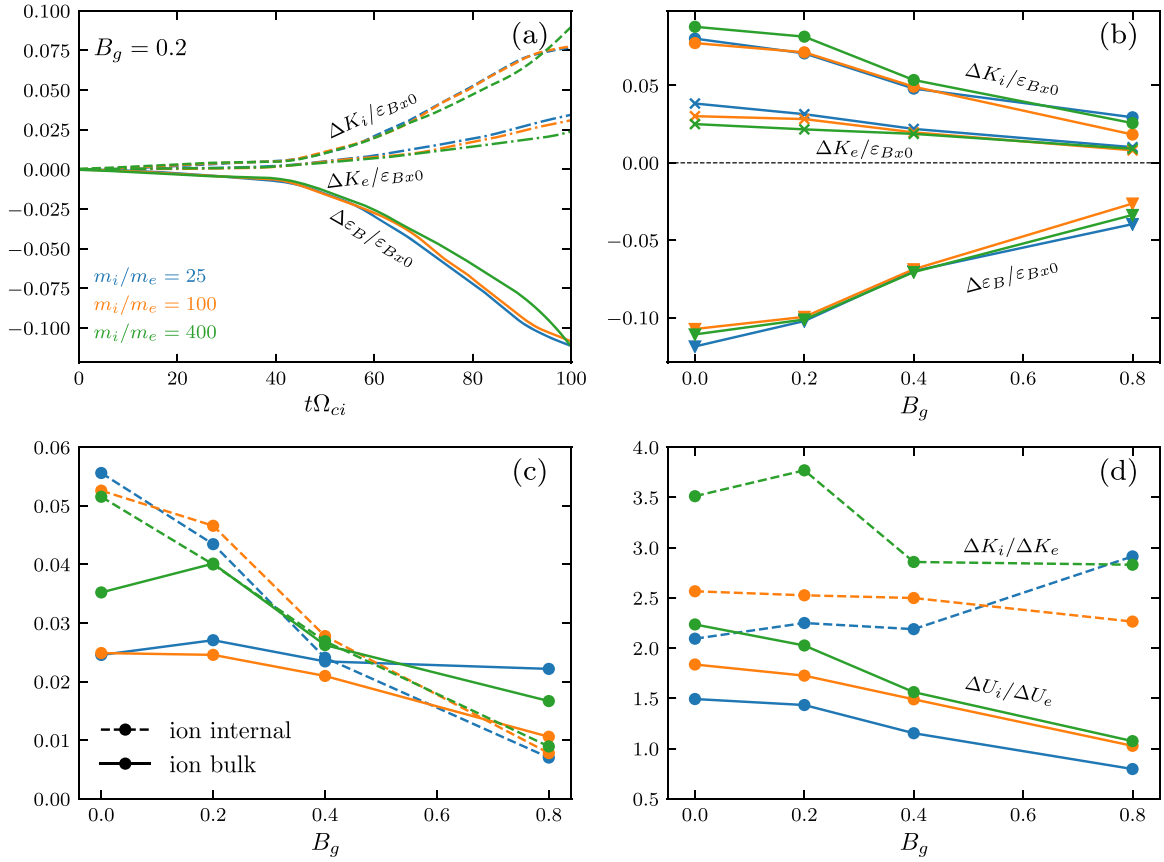

Figure 4. Energy conversion for different runs. (a) Time evolution of the change of the magnetic energy $\Delta\varepsilon_B$ (solid), the electron energy gain ΔK_e (dashed–dotted), and the ion energy gain ΔK_i (dashed) for the runs with $B_g = 0.2$. The energies are normalized by the initial energy of the reconnecting component of the magnetic field ε_{Bx0}. We have shifted the runs with $m_e/m_i = 100$ by $-3\Omega_{ci}^{-1}$ and the runs with $m_i/m_e = 400$ by $-6\Omega_{ci}^{-1}$ as described in Figure 3. (b) The changes of the magnetic energy (triangle), the electron energy gain (star), and the ion energy gain ΔU_i (circle) accumulated to $t\Omega_{ci} = 100$. (c) Ion internal energy gain and bulk energy gain. They are also normalized by ε_{Bx0}. The internal energy density is calculated from the diagonal components of the ion pressure tensor as $\sum_i P_{ii}/2$. The ion bulk energy density is $0.5 n_i m_i u_i^2$, where u_i is the ion bulk flow speed. (d) The energy partition between ions and electrons. The dashed lines are for the total kinetic energies; the solid lines are for the internal energies.

$\varepsilon \in [10, 100]\varepsilon_{\rm th}$, especially in the runs with $B_g = 0$ and 0.2 (panels (e) and (f)). But these spectra are actually the superposition of a series of thermal-like distributions in different sectors of a 2D magnetic island (Li et al. 2017). To the end of the simulations (panels (i)–(l)), the separation between different mass ratio becomes even larger. The spectra in the runs with $m_i/m_e = 25$ still appear to be power laws with power index -3.5, and the spectra are much steeper in the runs with higher mass ratios. These results indicate that a lower proton-to-electron mass ratio tends to overestimate the high-energy electron acceleration.

Figure 6 shows the normalized ion energy spectra for all ions at $t\Omega_{ci} = 40$, 60, and 94. Ions are accelerated up to $500\varepsilon_{\rm th}$, higher than electrons. The accelerated ions develop significant high-energy tails. At the beginning ($t\Omega_{ci} = 40$), ions are quickly accelerated to the reconnection outflow speed $\approx v_{\rm A}$. This process does not increase the ion internal energy much but rather accelerates all ions in the reconnection exhausts to a bulk kinetic energy of $0.5 m_i v_{\rm A}^2$. We find that the acceleration is associated with particle polarization drift instead of the parallel electric field as for electrons (more discussion in Figure 7). As the simulations evolve to $t\Omega_{ci} = 60$ (panels (e)–(h)), the spectra in the runs with $m_i/m_e = 25$ and 100 are close to each other, and the fluxes of high-energy ions in the runs with $m_i/m_e = 400$ are still lower. The spectra appear to be power laws $\propto\varepsilon^{-1}$ for ε around $10\varepsilon_{\rm th}$. The high-energy tail is likely a drift Maxwellian distribution with a drift energy $\approx 0.5 m_i v_{\rm A}^2$, because the break point of the spectra is about $0.5 m_i v_{\rm A}^2$ (vertical solid line in panel (f)). To the end of the simulations (panels (i)–(l)), the low-energy part is still a hard power law $\propto\varepsilon^{-1}$, and the high-energy tail becomes harder and resembles a power law $\propto\varepsilon^{-6}$. The spectra in the runs with $m_i/m_e = 400$ are still steeper when $B_g = 0.0$ or 0.2, but the difference is obvious only at the highest energies ($\varepsilon > 200\varepsilon_{\rm th}$). The spectra in the runs with $B_g = 0.4$ or 0.8 are close to each other. We find that high-energy particles ($>0.5 m_i v_{\rm A}^2$) are further accelerated by the *Fermi*-like mechanism associated with particle curvature drift (more discussion later). The maximum ion energy keeps increasing because of the *Fermi*-like mechanism but is limited by the simulation duration ($100\Omega_{ci}^{-1} \approx 16$ ion gyro-period). We expect that ions can be accelerated to higher energies and develop an even harder high-energy tail in larger simulations. In summary, ions develop similar energy spectra for different mass ratio, and the spectra have a hard low-energy part and a steep high-energy part, separating by the reconnection bulk flow energy $0.5 m_i v_{\rm A}^2$.

3.5. Plasma Energization

Plasma energization analysis based on the guiding-center drift description has been routinely carried out in kinetic simulations for studying particle acceleration mechanisms (Dahlin et al. 2014; Li et al. 2015, 2017, 2018a; Wang et al.

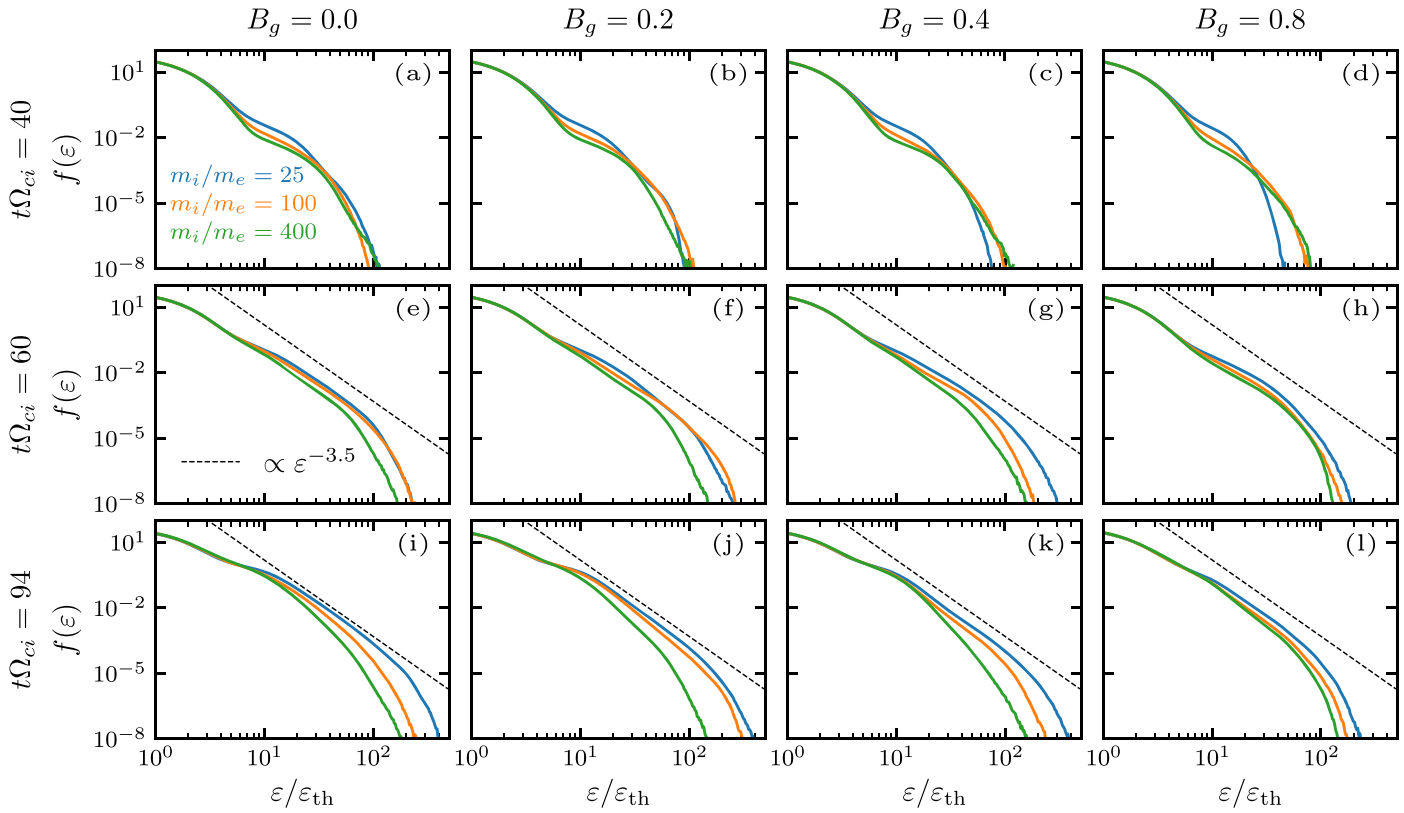

Figure 5. Normalized electron energy spectra $f(\varepsilon) = (dN(\varepsilon)/d\varepsilon)/(N_{\rm tot}\ \varepsilon_{\rm th}^{400}/\varepsilon_{\rm th})$ at $t\Omega_{ci} = 40$, 60, and 94, where $N_{\rm tot} \equiv n_x \times n_z \times$ nppc is the total number of macro electrons in the simulation, $\varepsilon_{\rm th} = 3kT_0/2$ is the initial thermal energy for different mass ratio, and $\varepsilon_{\rm th}^{400}$ is the initial thermal energy for $m_i/m_e = 400$. The electron kinetic energy $\varepsilon \equiv (\gamma - 1)m_e c^2$ is normalized by $\varepsilon_{\rm th}$, where γ is the Lorentz factor. Note that we shifted the runs with $m_i/m_e = 100$ by $-3\Omega_{ci}^{-1}$ and the runs with $m_i/m_e = 400$ by $-6\Omega_{ci}^{-1}$ to match the reconnection onset. The dashed lines indicate power-law distributions with a power index -3.5. Note that they are not fitted distributions but only a guide for the analysis.

2016). Figure 8 shows multiple plasma energization terms associated with the parallel or perpendicular electric field, flow compression or flow shear (see (2) for their definitions), curvature drift or gradient drift (see (1) for their definitions), flow inertia or magnetization (see (1) for their definitions), and gyrotropic or agyrotropic pressure tensors. For electrons, a mass ratio of 25 tends to overestimate the contributions by $\boldsymbol{E}_\perp$ (panel (a)), flow compression and shear (panel (b)), flow inertia (panel (d)), and gyrotropic pressure tensor (panel (e)), but the guide field dependence is consistent across runs with different mass ratios. Among these terms, the inertia term is mostly overestimated in the runs with $m_i/m_e = 25$, but it only contributes to the bulk energization. For ions, Figure 8(g) shows that $m_i/m_e = 25$ tends to overestimate the contribution by flow shear when $B_g \leqslant 0.2$, and that $m_i/m_e = 25$ or 100 tends to overestimate the contribution by flow compression when $B_g \leqslant 0.2$; Figure 8(j) shows that ions are more gyrotropic in the runs with $m_i/m_e = 25$ than that in the runs with a higher mass ratio. This is because ions become less well magnetized when its gyroradius $\rho_i/d_e = v_{\rm thi}\omega_{pe}/(c\Omega_{ci}) = \sqrt{m_i/m_e}(v_{\rm thi}/v_{\rm A})$ gets larger with the mass ratio, where $v_{\rm thi}/v_{\rm A} = \sqrt{\beta_i}$ is the same for all runs.

Since other energization terms were more or less studied before, we summarize the results shown in Figure 8 without going into details. For electrons, panel (a) shows that most energization is done by $\boldsymbol{E}_\perp$ when $B_g < 0.5$, and that the energization by $\boldsymbol{E}_\parallel$ becomes comparable with that by $\boldsymbol{E}_\perp$ when $B_g = 0.8$; panel (b) shows that flow compression energization dominates flow shear energization ($\propto$ pressure anisotropy), although the former keeps decreasing with the guide field, and the latter slightly increases until $B_g = 0.4$ because of an increasing pressure anisotropy (Li et al. 2018a); panels (c) and (d) show that the energization associated with curvature drift dominates the other energization terms by $\boldsymbol{E}_\perp$, and that the energization associated with flow inertia contributes significantly only when $m_i/m_e = 25$; panel (e) shows that the energization associated with the gyrotropic pressure tensor always dominates the energization associated with the agyrotropic pressure tensor, indicating that most electrons are well magnetized in the simulations. For ions, panel (f) shows that most energization is done by $\boldsymbol{E}_\perp$, and that this does not change much with the guide field; panel (g) shows that compression energization always dominates shear energization, and that both terms gradually decrease with the guide field, which is different from that for electrons; panels (h)–(j) show that the energization associated with curvature drift and flow inertia are the two most important terms for ions besides the energization associated with the agyrotropic pressure tensor, and that curvature drift dominates when $B_g < 0.4$ and flow inertia dominates when $B_g \geqslant 0.4$. In summary, plasma energization is similar in runs with different mass ratios, so a lower mass ratio (e.g., 25) is still useful for studying particle acceleration mechanisms and their scaling with the guide field.

3.6. Particle Acceleration Rates

To further reveal the difference between runs with different mass ratios, we use all particles to evaluate the particle acceleration rates $\alpha(\varepsilon, t) \equiv \langle \dot{\varepsilon}(\varepsilon, t)/\varepsilon(t)\rangle$ associated with $\boldsymbol{E}_\parallel$,

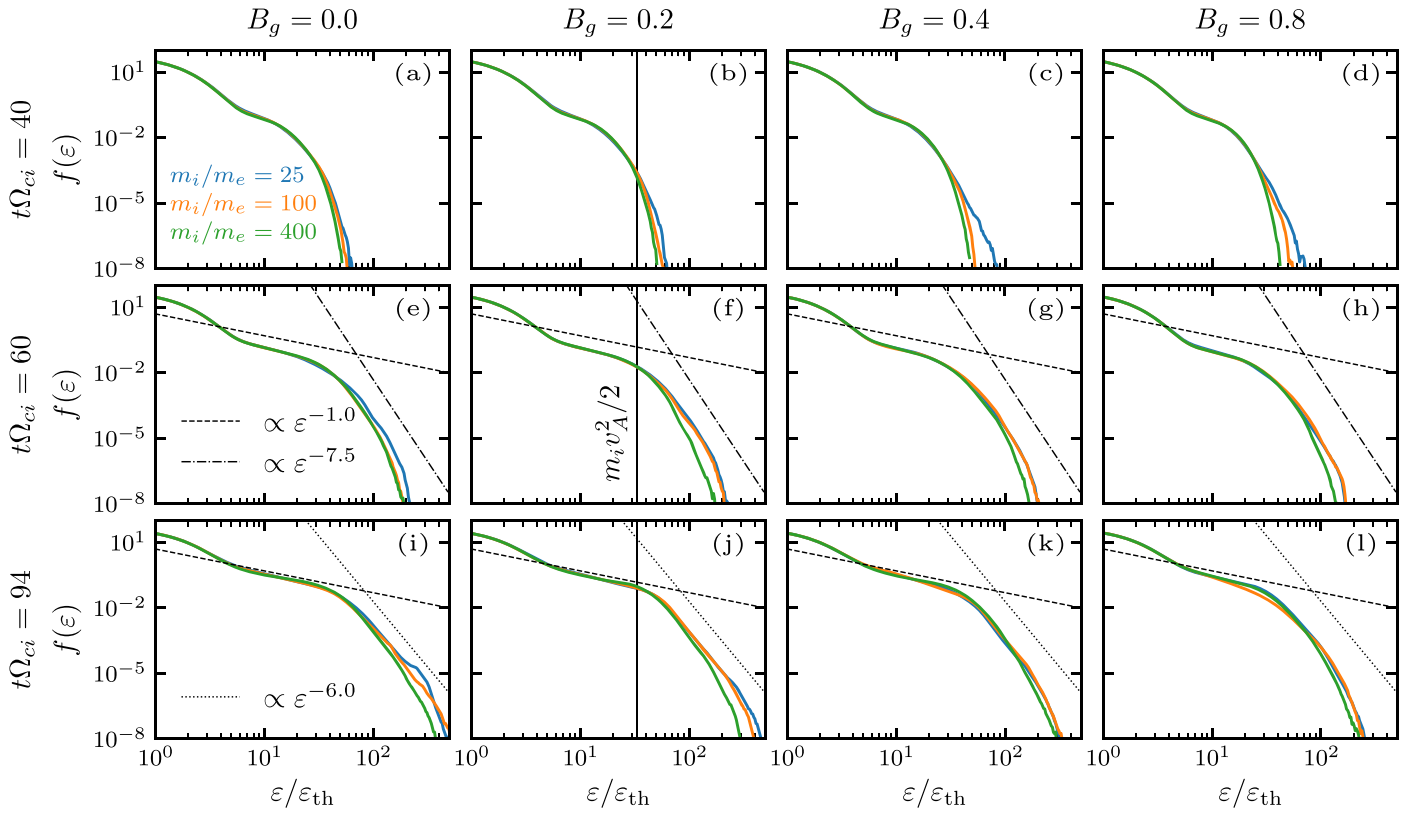

Figure 6. Normalized ion energy spectra $f(\varepsilon) = (dN(\varepsilon)/d\varepsilon)/(N_{\rm tot}\varepsilon_{\rm th}^{400}/\varepsilon_{\rm th})$ at $t\Omega_{ci} = 40$, 60, and 94, where $N_{\rm tot} \equiv n_x \times n_z \times$ nppc is the total number of macro ions in the simulation, $\varepsilon_{\rm th} = 3kT_0/2$ is the initial thermal energy for different mass ratio, and $\varepsilon_{\rm th}^{400}$ is the initial thermal energy for $m_i/m_e = 400$. The ion kinetic energy $\varepsilon \equiv (\gamma - 1)m_i c^2$ is normalized by $\varepsilon_{\rm th}$, where γ is the Lorentz factor. Note that we shifted the runs with $m_i/m_e = 100$ by $-3\Omega_{ci}^{-1}$ and the runs with $m_i/m_e = 400$ by $-6\Omega_{ci}^{-1}$ to match the reconnection onset. The dashed lines indicate power-law distributions with a power index -1.0. The dotted lines indicate power-law distributions with a power index -6.0. The dashed–dotted lines indicate power-law distributions with a power index -7.5. Note that they are not fitted distributions but only a guide for the analysis. The vertical black lines indicate the bulk kinetic energy of a single ion advected by the reconnection outflow ($\approx v_A$).

$\boldsymbol{E}_\perp$, curvature drift, gradient drift, parallel drift, inertial drift, polarization drift, and betatron acceleration. Figure 9 shows the two largest terms for electrons: $\boldsymbol{E}_\parallel$ and curvature drift, for the runs with $B_g = 0.2$. Since the simulation duration is $100\Omega_{ci}^{-1}$ for all runs, in order to compare among the runs with different mass ratios, we normalize α by Ω_{ci}. We find that $\boldsymbol{E}_\parallel$ is efficient at accelerating electrons early in the simulation ($t\Omega_{ci} = 40$), but it does not accelerate or even decelerates energetic electrons ($>10\varepsilon_{\rm th}$) later. The right panels of Figure 9 show that particle curvature drift generally leads to acceleration. It gradually decreases as the simulation evolves and approaches zero for high-energy electrons ($>30\varepsilon_{\rm th}$) in the runs with $m_i/m_e = 100$ or 400 but stays finite in the run with $m_i/m_e = 25$. Combining the negative acceleration rate due to $\boldsymbol{E}_\parallel$, we find that high-energy electrons are decelerated later in the runs with $m_i/m_e = 100$ or 400. In contrast, the high-energy electrons are continuously accelerated in the run with $m_i/m_e = 25$, so the "power law" can survive, as shown in Figure 5. Note that these results still hold for runs with different guide fields that are not shown here. In summary, as the mass ratio gets larger, high-energy electron acceleration becomes less efficient, because the acceleration rate by $\boldsymbol{E}_\parallel$ becomes negative, and because the *Fermi*-like mechanism becomes less efficient.

Figure 7 shows the acceleration rates for ions. We find that the acceleration rates associated with particle inertial drift, polarization drift, and curvature drift are most important for ions. Since the inertial drift contains particle curvature drift, we subtract the curvature drift from the inertial drift and call the residue the inertial' drift in the left panels. The acceleration rate associated with the inertial' drift is negative for energetic ions with tens of $\varepsilon_{\rm th}$, indicating that the acceleration process associated with the inertial' drift decelerates ions. The middle panels of Figure 7 show that α associated with polarization drift is efficiently at accelerating ions at different energies early in the simulations but peaks around $5\varepsilon_{\rm th}$ and approaches zero when $\varepsilon > 20\varepsilon_{\rm th}$ later in the simulations. This indicates that particle polarization drift along $\boldsymbol{E}_\perp$ is efficient at driving the reconnection bulk flow. In contrast, the right panels of Figure 7 show that the *Fermi*-like mechanism associated with particle curvature drift preferentially accelerates ions at high energies ($>20\varepsilon_{\rm th}$), and that it is still strong to the end of the simulations. We expect that ions can be accelerated to higher energies and develop an even harder high-energy spectra in larger simulations. The right panels show that the acceleration associated with curvature drift is slightly smaller in the run with $m_i/m_e = 400$ than that in the runs with lower mass ratios. This explains why the high-energy ion fluxes are lower in the runs with $m_i/m_e = 400$, as shown in Figure 6. These results on the ion acceleration rates are consistent among the runs with different mass ratio, suggesting that we could use a lower mass ratio (e.g., 25 or 100) to study ion acceleration in low-β reconnection.

4. Conclusions and Discussions

In this work, we study whether and how the proton-to-electron mass ratio affects the particle acceleration processes in kinetic simulations of magnetic reconnection through

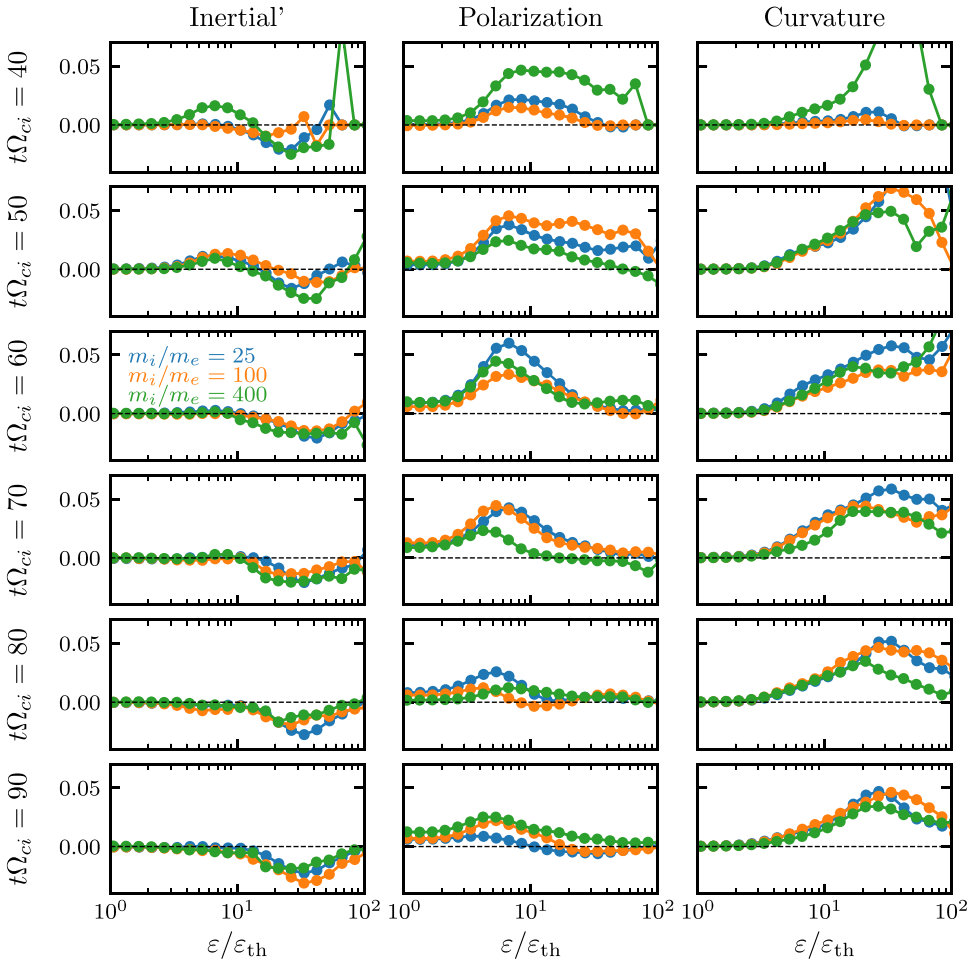

Figure 7. Ion acceleration rate $\alpha(\varepsilon, t) \equiv \langle \dot{\varepsilon}(\varepsilon, t)/\varepsilon(t) \rangle$ associated with particle inertial' drift defined as particle inertial drift subtracted by particle curvature, particle curvature drift, and particle polarization drift for the runs with $B_g = 0.2$, where $\langle \ldots \rangle$ is the average for particles in different energy bins. We normalize α by Ω_{ci} to compare among the runs with different mass ratios. Since we only have 10 time frames of particle data, we only shifted the run with $m_i/m_e = 400$ by $-10\Omega_{ci}^{-1}$.

performing simulations with different mass ratio and guide field strength. The simulations show different current layer structures that depend on the mass ratio and guide field strength, consistent with earlier studies (e.g., Le et al. 2013). We find that simulations with different mass ratios are similar in reconnection rate, magnetic energy conversion, ion internal energy gain, plasma energization processes, ion energy spectra, and the acceleration mechanisms for high-energy ions, but simulations show different electron internal energy gain, electron energy spectrum, and the acceleration efficiencies for high-energy electrons. We find that electrons gain more energy (internal or kinetic) in runs with lower mass ratios. As a result, the ion-to-electron energy partition increases with the mass ratio, e.g., from 1.5 for $m_i/m_e = 25$ to 2.25 for $m_i/m_e = 400$ when $B_g = 0$. We find that the electron spectrum gets steeper as the mass ratio gets larger. By calculating the particle acceleration rates due to different particle guiding-center drift motions, we find that as the mass ratio increases, high-energy electron acceleration becomes less efficient because parallel electric field tends to decelerate high-energy electrons, and because the *Fermi*-like mechanism associated with particle curvature drift becomes less efficient.

The simulations also show that the total plasma energization associated with the guiding-center drift motions and flow compression and shear is similar for the runs with different mass ratio. A lower mass ratio tends to overestimate some of the energization terms, but the guide field dependence is consistent across runs with different mass ratios. By subtracting the gyrotropic pressure tensor from the whole pressure tensor, we find that most electrons are well magnetized even when $B_g = 0$, and that the agyrotropic ion distributions contribute over 15% of the total ion energization when $m_i/m_e = 400$ and $B_g \geqslant 0.2$. This indicates that ions are not well magnetized when m_i/m_e is large. These results suggest that a lower mass ratio is still good for studying energy conversion mechanisms during magnetic reconnection.

The ion acceleration rates show that the acceleration terms associated with ion inertial drift, polarization drift, and curvature drift are most important for ions. Ion inertial drift (with curvature drift being subtracted) decelerates high-energy ions (>20 times of the initial thermal energy). Ion polarization drift tends to drive the reconnection bulk flow and is mostly efficient for low-energy ions (around 5 times the initial thermal energy). We find that high-energy ions are accelerated by the *Fermi*-like mechanism associated with particle curvature drift along the motional electric field.

The ion energy distributions show that ions are accelerated to form Alfvénic reconnection outflow when they enter the reconnection layer. The thermalization processes (e.g., compression and shear) result in a much hotter plasma than the

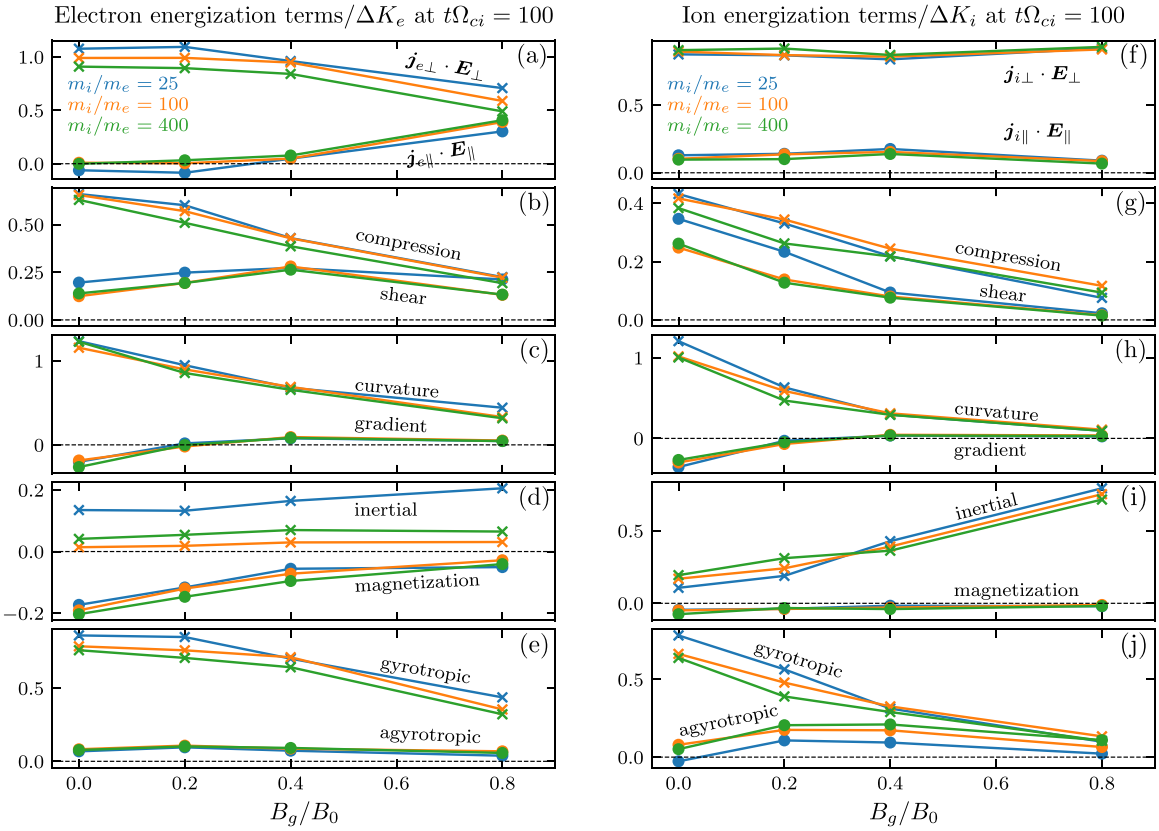

Figure 8. Fluid energization terms accumulated to $t\Omega_{ci} = 100$ for electrons (left panels) and ions (right panels). All these terms are integrated over the whole simulation domain and normalized by the particle energy gain (ΔK_e or ΔK_i) at $t\Omega_{ci} = 100$. ((a) and (f)) Energization by parallel or perpendicular electric field. ((b) and (g)) Energization associated with flow compression or flow shear (see (2) for their definitions). ((c) and (h)) Energization associated with curvature drift or gradient drift (see (1) for their definitions). ((d) and (i)) Energization associated with flow inertia or magnetization (see (1) for their definitions). ((e) and (j)) Energization associated with the gyrotropic pressure tensor $(\nabla \cdot \mathsf{P}_{gs}) \cdot \boldsymbol{v}_E$ or the agyrotropic pressure tensor $(\nabla \cdot \mathsf{P}_s - \nabla \cdot \mathsf{P}_{gs}) \cdot \boldsymbol{v}_E$, where P_s is the whole pressure tensor for a single species, $\mathsf{P}_{gs} \equiv p_{s\perp}\mathsf{I} + (p_{s\parallel} - p_{s\perp})\boldsymbol{bb}$ is gyrotropic pressure tensor, $p_{s\parallel}$ is the parallel pressure, $p_{s\perp}$ is the perpendicular pressure, I is the unit dyadic, $\boldsymbol{b}$ is the unit vector along the local magnetic field direction, and $\boldsymbol{v}_E$ is the $\boldsymbol{E} \times \boldsymbol{B}$ drift velocity. Note that the accumulation over time could introduce errors since we only have 100 time frames.

inflow plasma. Similar processes could occur in solar flares, where $v_A \approx 10^3\,\mathrm{km\,s^{-1}}$ and the ion thermal speed $v_{thi} \approx 10^2\,\mathrm{km\,s^{-1}}$ in the lower solar corona. As indicated by observations (e.g., Liu et al. 2013), the coronal plasma can be heated from 1 MK to tens of MK in a flare region. The superposition of such multicomponent super-hot plasmas can even produce the observed coronal hard X-ray emission, as predicted in simulations by Cheung et al. (2018).

We have carried out another set of simulations (Figure 10), in which we fix the electron thermal velocity and ω_{pe}/Ω_{ce} (effectively varying the Alfvén speed for different mass ratio). This is typical when using a lower mass ratio to save the computational costs. We find that the above conclusions still hold for this new set of simulations. The consistency between the two sets of simulations suggests once the scale separation between electrons and ions is fixed, the acceleration processes of a single species will be similar. Below is our explanation of similar ion acceleration and different electron acceleration in runs with different mass ratio. The particle acceleration rates (Figure 9 and 7) show particle curvature drift as the dominant high-energy acceleration mechanism, and the curvature drift acceleration is most efficient in the reconnection exhaust ($\sim d_i$). We can treat the d_i as the energy-containing scale. The closer the particle gyromotion scale is to d_i, the stronger the high-energy acceleration we expect. For ions, ρ_i/d_i (0.1 in our simulations) is larger than ρ_e/d_i, so ions tend to be accelerated to higher energies than electrons; ρ_i/d_i is constant for different mass ratio, so the ion spectra are similar for different mass ratios. For electrons, ρ_e/d_i gets smaller as the mass ratio increases, so high-energy electron acceleration gets weaker when m_i/m_e gets larger.

Although we present results only for runs with a guide field up to $0.8B_0$, we have performed simulations with a stronger guide field (1.6, 3.2, and $6.4B_0$), which are more relevant to particle acceleration due to quasi-2D turbulence or interacting small-scale flux ropes in the inner heliosphere (Smith et al. 2006; Zank 2014; le Roux et al. 2015; Hu et al. 2018). We find that ion acceleration is still similar for runs with different mass ratio, and electron acceleration is still less efficient as the mass ratio gets larger. As the guide field becomes larger than B_0, the parallel electric field becomes the dominant energization mechanism for electrons, but it is inefficient at accelerating energetic electrons, resulting in much lower high-energy electron fluxes; the acceleration associated polarization drift becomes the dominate energization mechanism for ions, but it drives ion bulk flow instead of accelerating high-energy ions. For both electrons and ions, the acceleration rate associated with particle curvature drift becomes lower as the guide field gets stronger, indicating that the acceleration timescale becomes longer. To fully evaluate the effect of curvature drift in the strong guide field reconnection, we need much larger simulations that

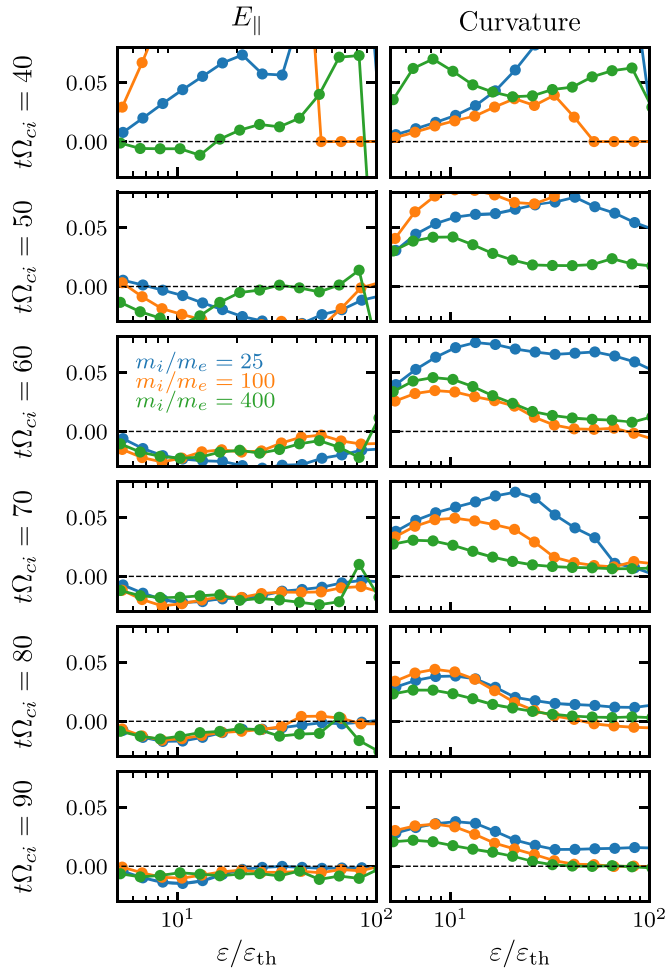

Figure 9. Electron acceleration rate $\alpha(\varepsilon, t) \equiv \langle \dot{\varepsilon}(\varepsilon, t)/\varepsilon(t)\rangle$ associated with the parallel electric field, and particle curvature drift for the runs with $B_g = 0.2$, where $\langle \ldots \rangle$ is the average for particles in different energy bins. We normalize α by Ω_{ci} to compare among the runs with different mass ratio. Since we only have 10 time frames of particle data, we only shifted the run with $m_i/m_e = 400$ by $-10\Omega_{ci}^{-1}$.

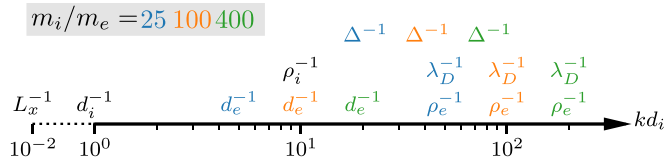

Figure 10. Similar to Figure 1 but for a different set of simulations, where we fix the electron thermal speed and ω_{pe}/Ω_{ce}. We use a lower resolution for runs with a lower m_i/m_e because λ_D is larger.

run for a much longer time. We defer these studies to a future work.

Our simulations have a few limitations. First, we perform simulations only in low-β plasmas with the same temperature for electrons and ions, which are suitable for studying particle acceleration at the reconnection site of a solar flare. Conclusions on the mass ratio dependence might change at the reconnection sites in Earth's magnetosphere or the accretion disk corona, where ions can be much hotter than electrons, and the plasma β can be larger than 0.1. Second, the simulation duration is limited by the box sizes and the periodic boundary conditions. A larger simulation with more realistic open boundary conditions could change the relative importance of the acceleration near the reconnection X-line and the acceleration associated with magnetic islands. Third, high-energy particles are confined in the 2D magnetic islands and cannot be further accelerated. The self-generated turbulence in 3D reconnection could change the acceleration processes and their dependence on the mass ratio.

To conclude, we find that different mass ratios are similar in reconnection rate, magnetic energy conversion, ion internal energy gain, plasma energization processes, ion energy spectra, and the acceleration mechanisms for high-energy ions. We find that ion acceleration is similar for different mass ratio because the dominant acceleration mechanism for energetic ions is due to particle curvature drift, and it does not change much with the mass ratio. Runs with different mass ratios are different in electron internal energy gain, electron energy spectrum, and the acceleration efficiencies for high-energy electrons. We find that high-energy electron acceleration becomes less efficient when the mass ratio gets larger because parallel electric field tends to decelerate high-energy electrons, and because the *Fermi*-like mechanism associated with particle curvature drift becomes less efficient. These results indicate that when particle curvature drift dominates high-energy particle acceleration, the further the particle kinetic scale are from the magnetic field curvature scales ($\sim d_i$), the weaker the acceleration will be, at least in 2D.

This work was supported by NASA grant NNH16AC60I. H.L. acknowledges the support by DOE/OFES. F.G.'s contribution is partly based upon work supported by the U.S. Department of Energy, Office of Fusion Energy Science, under Award No. DE-SC0018240. We also acknowledge support by the DOE through the LDRD program at LANL. We gratefully acknowledge our discussions with Bill Daughton, Ari Le, Adam Stanier, and Patrick Kilian. This research used resources provided by the Los Alamos National Laboratory Institutional Computing Program, which is supported by the U.S. Department of Energy National Nuclear Security Administration under Contract No. 89233218CNA000001, and resources of the National Energy Research Scientific Computing Center (NERSC), a U.S. Department of Energy Office of Science User Facility operated under Contract No. DE-AC02-05CH11231.

Appendix A
Fluid Description of Plasma Energization

Li et al. (2018a) described the plasma energization processes in terms of $\boldsymbol{j}_s \cdot \boldsymbol{E}$, where the perpendicular component of the current density $\boldsymbol{j}_s$ for any species is

$$\boldsymbol{j}_{s\perp} = p_{s\parallel}\frac{\boldsymbol{B}\times(\boldsymbol{B}\cdot\nabla)\boldsymbol{B}}{B^4} + p_{s\perp}\frac{\boldsymbol{B}\times\nabla B}{B^3} - \left[\nabla\times\frac{p_{s\perp}\boldsymbol{B}}{B^2}\right]_\perp + \rho_s\frac{\boldsymbol{E}\times\boldsymbol{B}}{B^2} - n_s m_s\frac{d\boldsymbol{u}_s}{dt}\times\frac{\boldsymbol{B}}{B^2}, \quad (1)$$

where $p_{s\parallel} = \langle(\boldsymbol{v}_\parallel - \boldsymbol{v}_{s\parallel})\cdot(\boldsymbol{p}_\parallel - \boldsymbol{p}_{s\parallel}/n_s)\rangle$ and $p_{s\perp} = 0.5\langle(\boldsymbol{v}_\perp - \boldsymbol{v}_{s\perp})\cdot(\boldsymbol{p}_\perp - \boldsymbol{p}_{s\perp}/n_s)\rangle$ are parallel and perpendicular pressures w.r.t the local magnetic field, respectively, ρ_s is the charge density, n_s is particle number density, m_s is particle mass, and $d/dt = \partial_t + \boldsymbol{v}_s\cdot\nabla$. In the language of particle drifts, the plasma energization is then associated with parallel electric field, curvature drift, gradient drift, magnetization, and flow

inertia. Li et al. (2018a) reorganized $\boldsymbol{j}_{s\perp}\cdot\boldsymbol{E}_{\perp}$ as

$$\boldsymbol{j}_{s\perp}\cdot\boldsymbol{E}_{\perp}=\nabla\cdot(p_{s\perp}\boldsymbol{v}_E)-p_s\nabla\cdot\boldsymbol{v}_E -(p_{s\parallel}-p_{s\perp})b_ib_j\sigma_{ij}+n_sm_s\frac{d\boldsymbol{u}_s}{dt}\cdot\boldsymbol{v}_E, \quad (2)$$

where $\boldsymbol{v}_E$ is the $\boldsymbol{E}\times\boldsymbol{B}$ drift velocity, $\sigma_{ij}=0.5\,(\partial_iv_{Ej}+\partial_jv_{Ei}-(2\nabla\cdot\boldsymbol{v}_E\delta_{ij})/3)$ is the shear tensor, and $p_s\equiv(p_{s\parallel}+2p_{s\perp})/3$ is the effective scalar pressure. Then, plasma energization is associated with parallel electric field, flow compression, flow shear, and flow inertia.

Appendix B
Drift Description of Particle Acceleration

Gyrophase-averaged particle guiding-center velocity is (Northrop 1963; le Roux & Webb 2009; Webb et al. 2009; le Roux et al. 2015)

$$\langle\boldsymbol{v}_g\rangle_\phi=v_\parallel\boldsymbol{b}+\boldsymbol{v}_E+\frac{M}{q_s}\frac{\boldsymbol{B}\times\nabla B}{B^2}+\frac{m_sv_\parallel}{q_sB}\boldsymbol{b} \times\frac{d\boldsymbol{b}}{dt}+\frac{M}{q_s}(\nabla\times\boldsymbol{b})_\parallel+\frac{m_s}{q_sB}\boldsymbol{b}\times\frac{d\boldsymbol{v}_E}{dt}, \quad (3)$$

where $d/dt=\partial/\partial t+(v_\parallel\boldsymbol{b}+\boldsymbol{v}_E)\cdot\nabla$, $M=m_s(\boldsymbol{v}_\perp-\boldsymbol{v}_E)^2/2B$ is particle magnetic moment in the plasma frame where $\boldsymbol{v}_E=0$. The terms on the right are the parallel guiding-center velocity, $\boldsymbol{E}\times\boldsymbol{B}$ drift, gradient drift, inertial drift (including curvature drift), parallel drift, and polarization drift. Assuming the perpendicular flow velocity $\boldsymbol{v}_{s\perp}\approx\boldsymbol{v}_E$ and particles are non-relativistic ($\boldsymbol{v}\approx\boldsymbol{p}/m_s$), the current density associated with particle gradient drift is

$$\int q_s\frac{M}{q_s}\frac{\boldsymbol{B}\times\nabla B}{B^2}fd^3p=p_{s\perp}\frac{\boldsymbol{B}\times\nabla B}{B^3}. \quad (4)$$

The current density associated with particle inertial drift is

$$\begin{aligned}&\int q_s\frac{m_sv_\parallel}{q_sB}\boldsymbol{b}\times\frac{d\boldsymbol{b}}{dt}fd^3p\\&=\int\frac{m_sv_\parallel}{B}\boldsymbol{b}\times\left(\frac{\partial\boldsymbol{b}}{\partial t}+(v_\parallel\boldsymbol{b}+\boldsymbol{v}_E)\cdot\nabla\boldsymbol{b}\right)fd^3p\\&=\frac{p_{s\parallel}+n_sm_sv_{s\parallel}^2}{B}\boldsymbol{b}\times(\boldsymbol{b}\cdot\nabla)\boldsymbol{b}+n_sm_s\frac{v_{s\parallel}}{B}\boldsymbol{b}\\&\quad\times\left(\frac{\partial\boldsymbol{b}}{\partial t}+(\boldsymbol{v}_E\cdot\nabla)\boldsymbol{b}\right)\\&=\frac{p_{s\parallel}}{B}\boldsymbol{b}\times(\boldsymbol{b}\cdot\nabla)\boldsymbol{b}+\frac{n_sm_s}{B}\boldsymbol{b}\times(\boldsymbol{v}_{s\parallel}\cdot\nabla)\boldsymbol{v}_{s\parallel}+\frac{n_sm_s}{B}\boldsymbol{b}\\&\quad\times\left(\frac{\partial}{\partial t}+\boldsymbol{v}_E\cdot\nabla\right)\boldsymbol{v}_{s\parallel}\\&=\frac{p_{s\parallel}}{B}\boldsymbol{b}\times(\boldsymbol{b}\cdot\nabla)\boldsymbol{b}+\frac{n_sm_s}{B}\boldsymbol{b}\times\left(\frac{\partial}{\partial t}+\boldsymbol{v}_s\cdot\nabla\right)\boldsymbol{v}_{s\parallel},\end{aligned} \quad (5)$$

where we get the current density associated with curvature drift and the flow inertial effect associated with the parallel component of the flow velocity. The current density associated with particle parallel drift is

$$\begin{aligned}&\int q_s\frac{M}{q_s}(\nabla\times\boldsymbol{b})_\parallel fd^3p\\&=\frac{p_{s\perp}}{B}(\nabla\times\boldsymbol{b})\cdot\boldsymbol{bb}\\&=\left(\nabla\times\frac{p_{s\perp}\boldsymbol{B}}{B^2}-\nabla\frac{p_{s\perp}}{B}\times\boldsymbol{b}\right)\cdot\boldsymbol{bb}\\&=-\left[\nabla\times\frac{p_{s\perp}\boldsymbol{B}}{B^2}\right]_\perp+\nabla\times\frac{p_{s\perp}\boldsymbol{B}}{B^2},\end{aligned} \quad (6)$$

where the first term is the current density associated with magnetization, and the dot product of the second term with $\boldsymbol{E}$ gives

$$\begin{aligned}&\left(\nabla\times\frac{p_{s\perp}\boldsymbol{B}}{B^2}\right)\cdot\boldsymbol{E}\\&=-\nabla\cdot(p_{s\perp}\boldsymbol{v}_E)+\frac{p_{s\perp}\boldsymbol{B}}{B^2}\cdot\nabla\times\boldsymbol{E}\\&=-\nabla\cdot(p_{s\perp}\boldsymbol{v}_E)-\frac{p_{s\perp}}{B}\frac{\partial B}{\partial t},\end{aligned} \quad (7)$$

where we used the Maxwell–Faraday equation, the first term cancels the first term on the right in Equation (2), and the second term cancels betatron acceleration. Finally, the energization associated with particle polarization drift is

$$\int q\frac{m_s}{qB}\boldsymbol{b}\times\frac{d\boldsymbol{v}_E}{dt}fd^3p=\frac{n_sm_s}{B}\boldsymbol{b}\times\left(\frac{\partial}{\partial t}+\boldsymbol{v}_s\cdot\nabla\right)\boldsymbol{v}_E, \quad (8)$$

which contributes to the flow inertial term. Combining Equations (4)–(8), we can reproduce Equation (1). The total plasma energization is

$$\int q_s\langle\boldsymbol{v}_g\rangle_\phi\cdot\boldsymbol{E}fd^3p+\frac{p_{s\perp}}{B}\frac{\partial B}{\partial t}=-p_s\nabla\cdot\boldsymbol{v}_E -(p_{s\parallel}-p_{s\perp})b_ib_j\sigma_{ij}+n_sm_s\frac{d\boldsymbol{u}_s}{dt}\cdot\boldsymbol{v}_E, \quad (9)$$

which is different from Equation (2) because of the terms in Equation (7). Table 1 compares the two descriptions.

Table 1
Comparing Particle Description and Fluid Description of the Energization Processes

Particle Description	Fluid Description (Equation (1))
Inertial drift (Equation (5))	curvature drift + part of flow inertial term
Curvature drift (part of inertial drift Equation (5))	curvature drift
Gradient drift (Equation (4))	gradient drift
Parallel drift + betatron acceleration (Equations (6) and (7))	magnetization
Polarization drift (Equation (8))	part of flow inertial term
Parallel guiding-center velocity	parallel flow velocity
$\boldsymbol{E}\times\boldsymbol{B}$ drift	$\boldsymbol{E}\times\boldsymbol{B}$ drift

ORCID iDs

Xiaocan Li https://orcid.org/0000-0001-5278-8029
Fan Guo https://orcid.org/0000-0003-4315-3755
Hui Li https://orcid.org/0000-0003-3556-6568

References

Adhikari, L., Khabarova, O., Zank, G. P., & Zhao, L. L. 2019, ApJ, 873, 72
Birn, J., Drake, J. F., Shay, M. A., et al. 2001, JGR, 106, 3715
Bowers, K. J., Albright, B. J., Yin, L., Bergen, B., & Kwan, T. J. T. 2008, PhPl, 15, 055703
Caspi, A., & Lin, R. P. 2010, ApJL, 725, L161
Cheung, M. C. M., Rempel, M., Chintzoglou, G., et al. 2018, NatAs, 3, 160
Dahlin, J. T., Drake, J. F., & Swisdak, M. 2014, PhPl, 21, 092304
Daughton, W., & Karimabadi, H. 2007, PhPl, 14, 072303
Daughton, W., Roytershteyn, V., Albright, B. J., et al. 2009, PhRvL, 103, 065004
Daughton, W., Scudder, J., & Karimabadi, H. 2006, PhPl, 13, 072101
Drake, J. F., Arnold, H., Swisdak, M., & Dahlin, J. T. 2019, PhPl, 26, 012901
Drake, J. F., Shay, M. A., Thongthai, W., & Swisdak, M. 2005, PhRvL, 94, 095001
Drake, J. F., Swisdak, M., Che, H., & Shay, M. A. 2006, Natur, 443, 553
Drake, J. F., Swisdak, M., & Fermo, R. 2013, ApJL, 763, L5
Du, S., Guo, F., Zank, G. P., Li, X., & Stanier, A. 2018, ApJ, 867, 16
Egedal, J., Daughton, W., & Le, A. 2012, NatPh, 8, 321
Egedal, J., Daughton, W., Le, A., & Borg, A. L. 2015, PhPl, 22, 101208
Egedal, J., Le, A., & Daughton, W. 2013, PhPl, 20, 061201
Fu, X. R., Lu, Q. M., & Wang, S. 2006, PhPl, 13, 012309
Guo, F., Li, H., Daughton, W., & Liu, Y.-H. 2014, PhRvL, 113, 155005
Guo, F., Liu, Y.-H., Daughton, W., & Li, H. 2015, ApJ, 806, 167
Hoshino, M., Mukai, T., Terasawa, T., & Shinohara, I. 2001, JGR, 106, 25979
Hu, Q., Zheng, J., Chen, Y., le Roux, J., & Zhao, L. 2018, ApJS, 239, 12
Ji, H., & Daughton, W. 2011, PhPl, 18, 111207
Krucker, S., & Battaglia, M. 2014, ApJ, 780, 107
Krucker, S., Hudson, H. S., Glesener, L., et al. 2010, ApJ, 714, 1108
Le, A., Egedal, J., Ohia, O., et al. 2013, PhRvL, 110, 135004
le Roux, J. A., & Webb, G. M. 2009, ApJ, 693, 534
le Roux, J. A., Zank, G. P., & Khabarova, O. V. 2018, ApJ, 864, 158
le Roux, J. A., Zank, G. P., Webb, G. M., & Khabarova, O. 2015, ApJ, 801, 112
le Roux, J. A., Zank, G. P., Webb, G. M., & Khabarova, O. V. 2016, ApJ, 827, 47
Li, X., Guo, F., Li, H., & Birn, J. 2018a, ApJ, 855, 80
Li, X., Guo, F., Li, H., & Li, G. 2015, ApJL, 811, L24
Li, X., Guo, F., Li, H., & Li, G. 2017, ApJ, 843, 21
Li, X., Guo, F., Li, H., & Li, S. 2018b, ApJ, 866, 4
Lin, R. P., & Hudson, H. S. 1976, SoPh, 50, 153
Liu, W., Chen, Q., & Petrosian, V. 2013, ApJ, 767, 168
Liu, W., Li, H., Yin, L., et al. 2011, PhPl, 18, 052105
Longcope, D. W., Des Jardins, A. C., Carranza-Fulmer, T., & Qiu, J. 2010, SoPh, 267, 107
Lu, Q., Wang, H., Huang, K., Wang, R., & Wang, S. 2018, PhPl, 25 072126
Montag, P., Egedal, J., Lichko, E., & Wetherton, B. 2017, PhPl, 24, 062906
Nalewajko, K., Uzdensky, D. A., Cerutti, B., Werner, G. R., & Begelman, M. C. 2015, ApJ, 815, 101
Northrop, T. G. 1963, The Adabatic Motion of Charged Particles No. 21 (New York: Interscience)
Oka, M., Ishikawa, S., Saint-Hilaire, P., Krucker, S., & Lin, R. P. 2013, ApJ, 764, 6
Oka, M., Krucker, S., Hudson, H. S., & Saint-Hilaire, P. 2015, ApJ, 799, 129
Oka, M., Phan, T.-D., Krucker, S., Fujimoto, M., & Shinohara, I. 2010, ApJ, 714, 915
Parker, E. N. 1965, P&SS, 13, 9
Shih, A. Y., Lin, R. P., & Smith, D. M. 2009, ApJL, 698, L152
Smith, C. W., Isenberg, P. A., Matthaeus, W. H., & Richardson, J. D. 2006, ApJ, 638, 508
Wang, H., Lu, Q., Huang, C., & Wang, S. 2016, ApJ, 821, 84
Webb, G. M., Le Roux, J. A., & Zank, G. P. 2009, in AIP Conf. Ser. 1183, Drift Kinetic Theory and Cosmic Rays, ed. X. Ao & G. Z. R. Burrows (Melville, NY: AIP), 85
Zank, G. P. 2014, Transport Processes in Space Physics and Astrophysics, Vol. 877 (Berlin: Springer), 185
Zank, G. P., Hunana, P., Mostafavi, P., et al. 2015, ApJ, 814, 137
Zank, G. P., le Roux, J. A., Webb, G. M., Dosch, A., & Khabarova, O. 2014, ApJ, 797, 28
Zhao, L.-L., Zank, G. P., Chen, Y., et al. 2019, ApJ, 872, 4
Zhao, L.-L., Zank, G. P., Khabarova, O., et al. 2018, ApJL, 864, L34
Zweibel, E. G., & Yamada, M. 2009, ARA&A, 47, 291